BREAKUP OF FLEXIBLE FIBRES IN HOMOGENEOUS ISOTROPIC TURBULENCE

Lucas Menez
Complex Fluids and Flows Unit
Okinawa Institute of Science and Technology
Okinawa 904-0495, Japan
lucas.menez@oist.jp

Stefano Olivieri
Department of Civil, Chemical and Environmental Engineering
University of Genova
Genova 16126, Italy
stefano.olivieri@unige.it

Andrea Mazzino
Department of Civil, Chemical and Environmental Engineering
University of Genova
Genova 16145, Italy
andrea.mazzino@unige.it

Marco Edoardo Rosti
Complex Fluids and Flows Unit
Okinawa Institute of Science and Technology
Okinawa 904-0495, Japan
marco.rosti@oist.jp

ABSTRACT

We perform a total of six hundred independent, fully coupled direct numerical simulations to characterise the breakup of flexible fibres in homogeneous isotropic turbulence. Different fibre lengths are considered, spanning the entire turbulent energy cascade to assess the impact of the multi scale nature of turbulence on breakup. This is complemented by varying fibre flexibility to cover the so-called overdamped and underdamped regimes of fibre dynamics. We show that both the amplitude and preferential location of bending differ fundamentally between these regimes, with direct implications for the fragmentation time scale and fragment size distribution. The probability of breakup is found to always follow an exponential law, with a time-independent failure rate that depends on fibre length and bending stiffness. The failure rate increases with fibre length in the overdamped regime, while remaining nearly independent of length in the underdamped regime. Our results suggest that, in the overdamped regime, breakup predominantly produces two fragments of same size, whereas in the underdamped regime fibres are more likely to break near their extremities, resulting in smaller fragments and a broader size distribution.

INTRODUCTION

Fibre breakup under hydrodynamic forces can occur across a vast range of scales, from the degradation of DNA (Choi *et al.*, 2002) to the fragmentation of marine litter (Brouzet *et al.*, 2021). A quantitative understanding of fibre fragmentation in turbulence is particularly relevant in the context of marine pollution and microplastic formation (Cózar *et al.*, 2014), where fibre size can span all length scales of the turbulent cascade (Kooi *et al.*, 2021). Understanding turbulence-induced breakup of flexible fibres first requires an understanding of their dynamics. Chiarini *et al.* (2024) and Marchioli *et al.* (2026) have recently reported significant progress in this area. Notably, Olivieri *et al.* (2022) performed extensive fully coupled Direct Numerical Simulations (DNS) to characterise the effects of elasticity, inertia, and concentration on fibre curvature, from sub-Taylor to integral scales. Although many studies have been dedicated to the fragmentation of solid particle aggregates in turbulent flows (Bäbler *et al.*, 2008; Babler *et al.*, 2015; Marchioli & Soldati, 2015; Gey *et al.*, 2025), the fragmentation of individual particles remains poorly understood, with only a few studies addressing polymer scission (Vanapalli *et al.*, 2006; Vincenzi *et al.*, 2021) and fibre fragmentation (Allende *et al.*, 2020; Brouzet *et al.*, 2021; Mazzino, 2026).

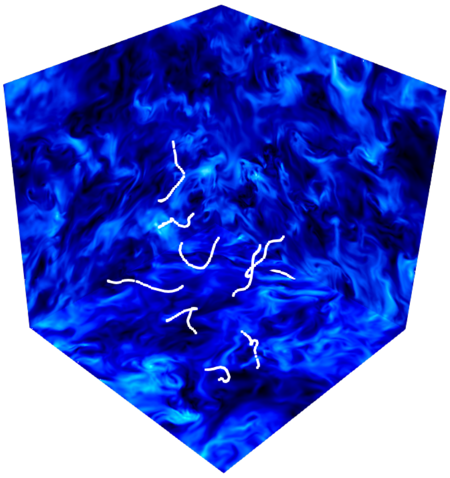

Figure 1: Visualisation of the flexible fibres (white lines) dispersed in the homogeneous isotropic turbulent flow. The magnitude of the instantaneous velocity field on three planes delimiting the fluid domain is shown in blue.

Under real conditions, microplastics fragmentation results from a prior increase in brittleness due to exposure to UV radiation, salt, ozone and living organisms (Andrady, 2011; DiBenedetto, 2026). Here, we study the breakup of flexible, brittle fibres in Homogeneous and Isotropic Turbulence (HIT) by means of DNS (see Figure 1). Previous studies have shown that breakup mechanisms are fundamentally different for *short* and *long* fibres. At dissipative scales, fibre dynamics follows that of stiff rods; breakup is primarily induced by buckling instability and is characterised by velocity-gradient statistics (Allende *et al.*, 2020). In the inertial subrange of turbulence, fibres may undergo flexural failure due to interactions with eddies of comparable size. Assuming fibres of moderate flexibility in the overdamped regime (Rosti *et al.*, 2018), Brouzet *et al.* (2021) reported that longer fibres are more likely to break than shorter ones, and that the fragmentation scenario ceases when fragments reach a physical cut-off length set by the fluid-structure interaction. More recently, again in the overdamped limit, Mazzino (2026) connected hydrodynamic loading to fibre curvature and eventually fracture, and identified two distinct breakup regimes separated by a critical fibre length. In the subcritical regime, breakup is a rare event and becomes more likely with increasing fibre length, whereas in the supercritical regime, breakup is frequent and becomes less likely as fibre length increases.

Here, we first characterise fibre curvature and identify two distinct behaviours depending on the ratio between the relaxation time of the fibre and the eddy turnover time at the fibre scale (overdamped/underdamped regimes). We then analyse the breakup process across turbulent scales and examine the role of bending stiffness from highly flexible to nearly rigid fibres.

METHODS

We perform fully coupled DNS of $N = 10$ fibres dispersed in HIT. The fibres are modelled as one-dimensional slender objects, characterised by their length c, their bending stiffness γ, and the difference in linear density between the solid and the fluid, $\Delta\tilde{\rho}$. Fibre dynamics follow the Euler–Bernoulli beam equation for an elastic filament, combined with the inextensibility constraint,

$$\Delta\tilde{\rho}\ddot{\boldsymbol{X}} = \partial_s(T\partial_s\boldsymbol{X}) - \gamma\partial_s^4\boldsymbol{X} - \boldsymbol{F}^{fs}, \tag{1}$$

$$\partial_s\boldsymbol{X}\cdot\partial_s\boldsymbol{X} = 1, \tag{2}$$

where $\boldsymbol{X}$ is the material point of the fibre corresponding to the curvilinear coordinate s, T is the tension enforcing the inextensibility constraint and $\boldsymbol{F}^{fs}$ is the fluid-solid interaction forcing term accounting for the force exerted by the fluid on the fibre. Brittle fragmentation essentially occurs when local stress overcomes the internal cohesion between molecules. Hence, we assume that the fibres can break under flexural failure when local curvature exceeds the critical curvature κ_c.

The fluid domain is a cube of size $L = 2\pi$ with periodic boundary conditions (see Figure 1). The dynamics of the carrier flow is governed by the Navier–Stokes equations for an incompressible flow and a Newtonian fluid,

$$\partial_t\boldsymbol{u} + \nabla\cdot\boldsymbol{u}\boldsymbol{u} = -\nabla p/\rho_f + \nu\nabla^2\boldsymbol{u} + \boldsymbol{f}^{turb} + \boldsymbol{f}^{fs}, \tag{3}$$

$$\nabla\cdot\boldsymbol{u} = 0, \tag{4}$$

where $\boldsymbol{u}$ and p are the velocity and pressure fields, respectively; ρ_f is the fluid density and ν is its kinematic viscosity, $\boldsymbol{f}^{turb}$ is the external forcing sustaining the turbulent flow (Eswaran & Pope, 1988) and $\boldsymbol{f}^{fs}$ is the fluid-solid interaction forcing term accounting for the back reaction of the fibres on the flow.

Flow and fibre dynamics are coupled through a no-slip condition, $\dot{\boldsymbol{X}} = \boldsymbol{u}$. The solid sub problem is solved using the numerical method detailed in Huang *et al.* (2007) and Banaei *et al.* (2020). The fluid sub problem is solved on a uniform Cartesian grid using a second-order central finite-difference method for spatial discretisation and a second-order Adams–Bashforth scheme is employed for time integration. The grid size is chosen such that $\Delta x = O(\eta)$, where η is the Kolmogorov length scale. Both sub problems are fully coupled through the terms $\boldsymbol{F}^{fs}$ and $\boldsymbol{f}^{fs}$ in equations (1) and (3), using the Immersed Boundary Method (IBM) proposed by Huang *et al.* (2007) and further modified by Banaei *et al.* (2020). More information about the in-house solver *Fujin* can be found in Rosti (2026).

Initially, the fibres are randomly dispersed in the fully-developed turbulent carrier flow, characterised by a Taylor micro-scale Reynolds number $Re_\lambda = u_{\mathrm{rms}}\lambda/\nu \simeq 157$, where u_{rms} is the root-mean-square velocity and λ is the Taylor micro-scale. Five different fibre lengths are considered, $c = \{0.1, 0.25, 0.5, 1, 2\}$, corresponding to $c/\eta \simeq \{9, 23, 47, 93, 186\}$. The fibres are respectively discretised into 4, 10, 16, 32 and 64 Lagrangian points, such that the Lagrangian mesh size matches the Eulerian one. The wave numbers associated with the different fibre lengths are indicated on the energy spectrum of the single-phase turbulent flow in Figure 2, highlighting that they span the entire turbulent cascade. Additionally, we consider four different values for the bending

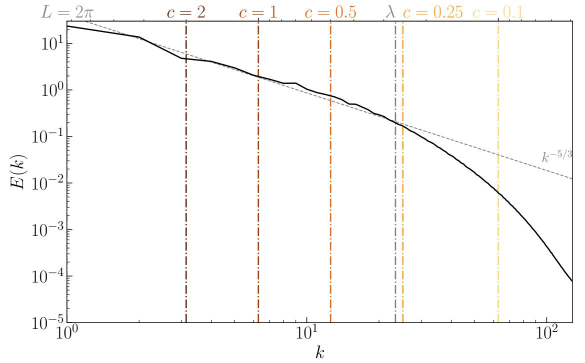

Figure 2: Energy spectrum of the turbulent single-phase flow (black line). The wave numbers k corresponding to the five fibre lengths c are shown as vertical coloured dash-dotted lines.

stiffness, $\gamma = \{10^{-8}, 10^{-4}, 10^{-2}, 10^{0}\}$, for a total of twenty independent cases. The fibres are highly flexible for $\gamma = 10^{-8}$ and almost rigid for $\gamma = 10^{0}$. The fibres are neutrally buoyant, with the difference in linear density between the solid and the fluid set to $\Delta\tilde{\rho} = 10^{-3}$. To achieve converged breakup statistics, thirty independent realisations of each case are performed, leading to a total of six hundred simulations. Each realisation is conducted with different initial fibres positions and orientations and independent flow initialisations.

RESULTS

The mean value of the local curvature, $\langle\kappa\rangle$, is shown in Figure 3 as a function of the curvilinear coordinate s, normalised by the fibre length c. The data are averaged over time, fibres and realisations. For conciseness, only the $\gamma = 10^{-8}$ (squares) and $\gamma = 10^{-2}$ (bullets) cases are represented. Overall, curvature increases as bending stiffness decreases. For sufficiently short fibres ($c \leq 1$) of low flexibility ($\gamma = 10^{-2}$), fibres are statistically more curved when increasing c, whereas the opposite behaviour is observed for high flexibility ($\gamma = 10^{-8}$). Dynamics of flexible fibres in turbulence can be classified into the so-called overdamped and underdamped regimes. In the overdamped regime, fibres are slaved to turbulence, whereas in the underdamped regime, fibre dynamics is dominated by elasticity or turbulence depending on the value of rigidity (Rosti *et al.*, 2018). The transition from the first to second regime arises when fibres cease to relax diffusively under viscous drag. This happens when the relaxation time of the fibre, $\tau_\mu = \mu c^4/\gamma$, becomes larger than the eddy turnover time at scale c, $\tau_c = \varepsilon^{-1/3} c^{2/3}$, where μ is the dynamic viscosity of the fluid and ε is the turbulent energy dissipation rate. Figure 4 provides a classification of the different cases into overdamped and underdamped regimes, based on the ratio τ_μ/τ_c. The overdamped and underdamped regimes give rise to two distinct bending behaviours, characterised by differences in both amplitude and preferential location along the fibre. For $\gamma = 10^{-2}$, the transition from overdamped to underdamped regimes occurs between $c = 0.5$ and $c = 1$ (see Figure 4). Consequently, both the amplitude and preferential location of bending are impacted (see Figure 3). For $\gamma = 10^{-8}$, all suspensions are in the underdamped regime, resulting in a monotonic trend.

Over the full range of parameters, fibres in the overdamped regime exhibit more important bending with increasing length, whereas the opposite trend is observed in the un-

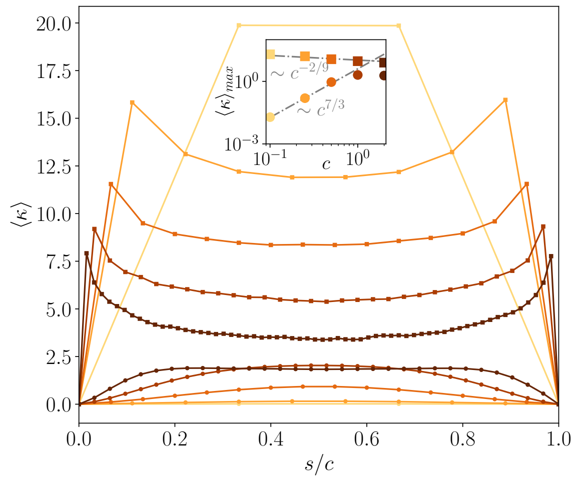

Figure 3: Mean of the local curvature as a function of the normalised curvilinear coordinate s/c. The inset shows the maximum value for each case as a function of the fibre length c. Colours: — $c = 0.1$; — $c = 0.25$; — $c = 0.5$; — $c = 1$; — $c = 2$. Symbols: ■ $\gamma = 10^{-8}$; • $\gamma = 10^{-2}$.

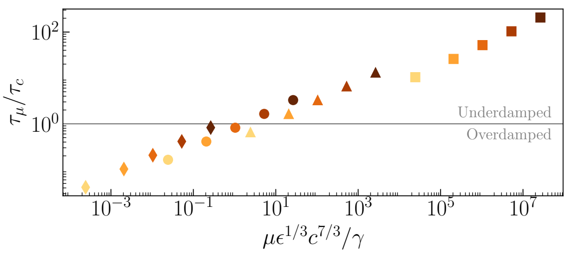

Figure 4: Ratio between the fibre relaxation time, τ_μ, and the eddy turnover time at scale c, τ_c, for all cases. For $\tau_\mu/\tau_c \ll 1$, fibres are in the overdamped regime, whereas for $\tau_\mu/\tau_c \gg 1$, they are in the underdamped regime. Colours: — $c = 0.1$; — $c = 0.25$; — $c = 0.5$; — $c = 1$; — $c = 2$. Symbols: ■ $\gamma = 10^{-8}$; ▲ $\gamma = 10^{-4}$; • $\gamma = 10^{-2}$; ◆ $\gamma = 10^{0}$.

derdamped regime. The inset in Figure 3 shows the maximum value of the mean curvature, which indeed exhibits markedly different trends for $\gamma = 10^{-2}$ and $\gamma = 10^{-8}$. For the more rigid fibres ($\gamma = 10^{-2}$), the maximum curvature increases as $\sim c^{7/3}$ from $c = 0.1$ to $c = 0.5$, consistently with the theoretical prediction of Mazzino (2026) in the overdamped regime, as well as the numerical results of Olivieri *et al.* (2022). Then, it transitions between $c = 0.5$ and $c = 1$ and eventually decreases as $\sim c^{-2/9}$. This power-law decay is consistent with the prediction of Gay *et al.* (2018) in the underdamped regime. This departure coincides with the aforementioned transition from overdamped to underdamped regimes. Dimensional analysis provides an estimate of the transition length between the weakly and highly flexible regimes via the non linear viscoelastic length scale (Marchioli *et al.*, 2026),

$$L_v = \frac{\gamma^{3/10}}{\mu^{3/10}\varepsilon^{1/10}}, \tag{5}$$

For $\gamma = 10^{-2}$, equation (5) yields $L_v \approx 0.61$, in well agree-

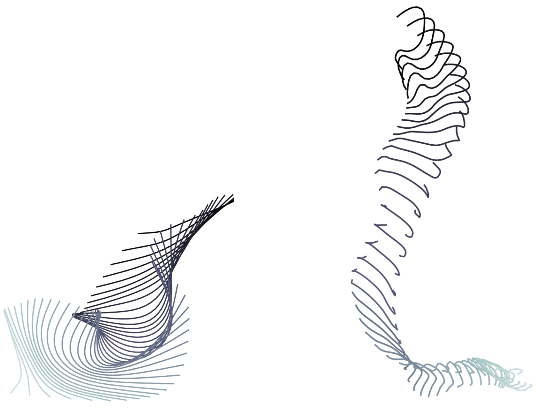

(a) overdamped (b) underdamped

Figure 5: Visualisation of the trajectory and deformation of a single fibre in the (a) overdamped regime ($c = 1$, $\gamma = 10^{-2}$) and (b) underdamped regime ($c = 1$, $\gamma = 10^{-8}$).

ment with the transition length identified in the inset of Figure 3 ($0.5 < L_v < 1$). A similar transition is also observed for $\gamma = 10^{-4}$ (not shown) and the predicted transition length again shows good agreement with the simulations. Our numerical results further confirm the validity of the non linear viscoelastic length scale in predicting the bending regime. For the most flexible fibres ($\gamma = 10^{-8}$), the maximum curvature decreases consistently as $\sim c^{-2/9}$. This monotonic behaviour arises because all suspensions operate in a single regime (underdamped) for $\gamma = 10^{-8}$. Indeed, for $\gamma = 10^{-8}$, equation (5) yields $L_v \approx 0.01$, which is of the order of the Kolmogorov length scale and one order of magnitude smaller than the smallest fibre length considered here.

Additionally, Figure 3 shows that the maximum curvature preferentially occurs at the fibres centre in the overdamped regime, whereas it is located near the extremities in the underdamped regime. These two distinct behaviours are illustrated by the trajectory and deformation of a single fibre in Figure 5. Unlike the overdamped regime where the fibre bends near its centre, the underdamped regime exhibits a straighter fibre configuration and stronger bending near the extremities. This mechanism was also observed experimentally by Gay *et al.* (2018) and attributed to fibre inextensibility and cumulative viscous effects. This suggests that fibres in the overdamped regime are more likely to break in their centre into two fragments of same size. In the underdamped regime, fibres are expected to break near their extremities, potentially leading to smaller fragments and a broader fragment size distribution.

Having characterised the fibre flexural behaviour, we now consider the first fragmentation event. Fibre breakup is assumed to occur when the curvature exceeds the critical value $\kappa_c = 20$. The survival function, denoted by S_κ, is shown in Figure 6a for all cases. It corresponds to the probability that a fibre survives beyond time t without undergoing failure. Note that this is also the Cumulative Distribution Function (CDF) of the breakup probability. Each point of coordinates $(t, S_\kappa(t))$ is obtained after detecting a breakup event, i.e., $\kappa(t) \geq \kappa_c$. Re-

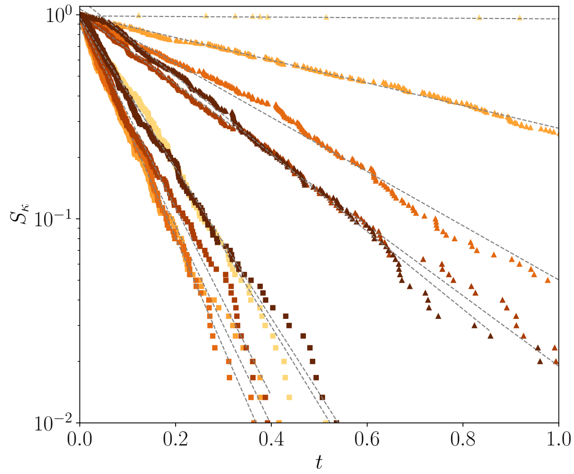

(a) Survival function

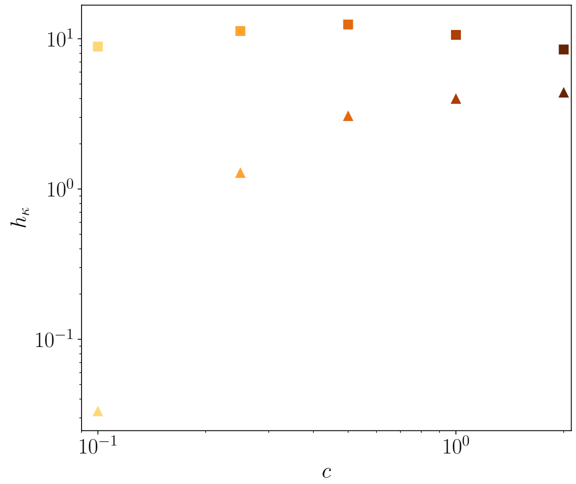

(b) Breakup hazard

Figure 6: (a) Survival function corresponding to the probability for a fibre to survive beyond time t. (b) Breakup hazard (or failure rate), computed from the survival function. The critical curvature is set to $\kappa_c = 20$. Colours: — $c = 0.1$; — $c = 0.25$; — $c = 0.5$; — $c = 1$; — $c = 2$. Symbols: ■ $\gamma = 10^{-8}$; ▲ $\gamma = 10^{-4}$.

markably, fibres do not break for $\gamma = 10^{-2}$ and $\gamma = 10^0$, as the critical curvature is not reached. Overall, the survival function exhibits exponential decay over time with a constant failure rate (over time) that depends on fibre length and bending stiffness. A similar trend was reported for drop breakup (Vela-Martín & Avila, 2022) and polymer scission (Vincenzi *et al.*, 2021) in turbulence, where the failure rate depends only on the Weber and Weissenberg numbers, respectively. As a first observation, the breakup process is accelerated for more flexible fibres here. More quantitatively, the breakup hazard h_κ (or failure rate) is obtained by performing a linear fitting of $\log(S_\kappa)$ (see gray dashed lines in Figure 6a) and is reported in Figure 6b for each case. It provides insight into how fast the fragmentation process occurs and its dependence on fibre length and bending stiffness. For the most flexible fibres ($\gamma = 10^{-8}$), the failure rate is maximal and remains largely independent of fibre length, exhibiting only a slight increase followed by a decrease, with a peak at $c = 0.5$. The decline at larger c may result from the slight reduction in bending observed for increasingly long fibres in the underdamped regime (see Figure 3). Conversely, the lower failure rate for shorter fibres indicates that, although they bend with a higher amplitude in average, high-curvature events are less likely to occur. Therefore, these violent and rare events may be linked to turbulence intermittency. Further work based on the recent theory of Mazzino (2026) may clarify the behaviour of smaller fibres in the dissipation range. For $\gamma = 10^{-4}$, the failure rate increases rapidly for shorter fibres before saturating for longer ones. This behaviour may originate from the transition between the overdamped and underdamped regimes, occurring between $c = 0.1$ and $c = 0.25$. As fibres do not break for $\gamma = 10^{-2}$ and $\gamma = 10^{0}$, the breakup hazard is zero in these cases.

SUMMARY

Previous studies have focused on the fragmentation of sub-Kolmogorov fibres due to buckling (Allende *et al.*, 2020) or fibres with length comparable to the integral scale (Brouzet *et al.*, 2021). However, a full understanding of fibre breakup across the entire turbulent energy spectrum is still lacking. Here, we performed a total of six hundred independent, fully coupled DNS to provide a comprehensive analysis of fibre breakup in HIT, covering fibre lengths across the entire turbulent energy cascade, as well as bending stiffness ranging from highly flexible to nearly rigid.

First, we have shown that the flexural behaviour of fibres can follow two distinct modes according to the so-called overdamped and underdamped regimes. In the overdamped regime, longer fibres bend more than shorter ones, and high curvature preferentially occurs at their centre. In contrast, in the underdamped regime, shorter fibres bend slightly more than longer ones, and undergo higher curvature near their extremities. Scaling predictions in both regimes, as well as an estimate of the transition length, have been confirmed by our numerical simulations. This work thus provides a unified picture of the flexural behaviour of fibres in turbulence across all scales of the energy cascade, encompassing both the overdamped regime and the largely unexplored underdamped regime.

Second, we revealed that the probability of fibre breakup in turbulence follows an exponential law with a time-independent failure rate, similarly to drop breakup or polymer scission. The fragmentation process is faster and almost independent of fibre length for highly flexible fibres. For moderate flexibility, the failure rate increases with fibre length and then saturates for the longest fibres, due to fibre straightening in the underdamped regime. The curvature analysis suggests that, in the overdamped regime, breakup leads to two fragments of same size. In contrast, in the underdamped regime, fibres are more likely to break near their extremities, forming smaller fragments and a broader size distribution.

In contrast to the breakup of sub-Kolmogorov fibres (Allende *et al.*, 2020), polymer scission (Vincenzi *et al.*, 2021), or bubble breakup (Vela-Martín & Avila, 2022) in turbulence, the flexural breakup of finite-size fibres appears to be significantly more complex. The dependence of the failure rate on fibre length c, bending stiffness γ, and critical curvature κ_c remains to be further quantified. Our ultimate goal is therefore to validate the recent theory of Mazzino (2026) in the overdamped regime using our numerical simulations, and to extend these findings to the underdamped regime.

REFERENCES

Allende, S., Henry, C. & Bec, J. 2020 Dynamics and fragmentation of small inextensible fibres in turbulence. *Philosophical Transactions of the Royal Society A: Mathematical, Physical and Engineering Sciences* **378** (2175), 20190398.

Andrady, A. L. 2011 Microplastics in the marine environment. *Marine Pollution Bulletin* **62** (8), 1596–1605.

Babler, M. U., Biferale, L., Brandt, L., Feudel, U., Guseva, K., Lanotte, A. S., Marchioli, C., Picano, F., Sardina, G. & Soldati, A. et al. 2015 Numerical simulations of aggregate breakup in bounded and unbounded turbulent flows. *Journal of Fluid Mechanics* **766**, 104–128.

Banaei, A. A., Rosti, M. E. & Brandt, L. 2020 Numerical study of filament suspensions at finite inertia. *Journal of Fluid Mechanics* **882**, A5.

Brouzet, C., Guiné, R., Dalbe, M.-J., Favier, B., Vandenberghe, N., Villermaux, E. & Verhille, G. 2021 Laboratory model for plastic fragmentation in the turbulent ocean. *Physical Review Fluids* **6**, 024601.

Bäbler, M. U., Morbidelli, M. & Bałdyga, J. 2008 Modelling the breakup of solid aggregates in turbulent flows. *Journal of Fluid Mechanics* **612**, 261–289.

Chiarini, A., Rosti, M. E. & Mazzino, A. 2024 Dynamics and applications of finite-size fibre-like objects in turbulent flows. *European Journal of Mechanics - B/Fluids* **108**, 104–118.

Choi, H. J., Lim, S. T., Lai, P.-Y. & Chan, C. K. 2002 Turbulent drag reduction and degradation of DNA. *Physical Review Letters* **89**, 088302.

Cózar, A., Echevarría, F. & et al., J. I. González-Gordillo 2014 Plastic debris in the open ocean. *Proceedings of the National Academy of Sciences* **111** (28), 10239–10244.

DiBenedetto, M. H. 2026 The fluid mechanics of ocean microplastics. *Annual Review of Fluid Mechanics* **58** (2026), 355–382.

Eswaran, V. & Pope, S. B. 1988 An examination of forcing in direct numerical simulations of turbulence. *Computers & Fluids* **16** (3), 257–278.

Gay, A., Favier, B. & Verhille, G. 2018 Characterisation of flexible fibre deformations in turbulence. *Europhysics Letters* **123** (2), 24001.

Gey, L., Le Gal, P. & Verhille, G. 2025 Formation and fragmentation of nylon fibre aggregates. *Proceedings of the Royal Society A: Mathematical, Physical and Engineering Sciences* **481** (2318), 20250246.

Huang, W.-X., Shin, S. J. & Sung, H. J. 2007 Simulation of flexible filaments in a uniform flow by the immersed boundary method. *Journal of Computational Physics* **226** (2), 2206–2228.

Kooi, M., Primpke, S., Mintenig, S. M., Lorenz, C., Gerdts, G. & Koelmans, A. A. 2021 Characterizing the multidimensionality of microplastics across environmental compartments. *Water Research* **202**, 117429.

Marchioli, C., Rosti, M. E. & Verhille, G. 2026 Flexible fibers in turbulence. *Annual Review of Fluid Mechanics* **58**, 167–192.

Marchioli, C. & Soldati, A. 2015 Turbulent breakage of ductile aggregates. *Physical Review E* **91**, 053003.

Mazzino, A. 2026 Turbulence-informed kinetic theory of inertial-range fibre fragmentation. *Journal of Fluid Mechanics* **1030**, A6.

Olivieri, S., Mazzino, A. & Rosti, M. E. 2022 On the fully coupled dynamics of flexible fibres dispersed in modulated turbulence. *Journal of Fluid Mechanics* **946**, A34.

Rosti, M. E. 2026 Simulating laminar and turbulent multiphase flows with fujin. *Fluid Dynamics Research* **58** (2), 021401.

Rosti, M. E., Banaei, A. A., Brandt, L. & Mazzino, A. 2018 Flexible fiber reveals the two-point statistical properties of turbulence. *Physical Review Letters* **121**, 044501.

Vanapalli, S. A., Ceccio, S. L. & Solomon, M. J. 2006 Universal scaling for polymer chain scission in turbulence. *Proceedings of the National Academy of Sciences* **103** (45), 16660–16665.

Vela-Martín, A. & Avila, M. 2022 Memoryless drop breakup in turbulence. *Science Advances* **8** (50), eabp9561.

Vincenzi, D., Watanabe, T., Ray, S. S. & Picardo, J. R. 2021 Polymer scission in turbulent flows. *Journal of Fluid Mechanics* **912**, A18.